Journal of
Composites Science

MDPI

Article

Fracture Toughening of Carbon Fiber Composites Based on Electrospun Nanofiber Interleafs

Matthias Schär [1,*], Ata Yoosefinejad [2], Naresh Sanandiya [2], Hamed Heravi [3], Peyman Adl [3], Frederick Tischhauser [4], Edgars Eglitis [4], Mohammad Hajikazemi [1] and Christian Brauner [1]

[1] Institute of Polymer Engineering, FHNW University of Applied Sciences and Arts Northwestern Switzerland, Klosterzelgstrasse 2, 5210 Windisch, Switzerland; mohammad.hajikazemi@fhnw.ch (M.H.); christian.brauner@fhnw.ch (C.B.)
[2] Munro Technology Limited, Lufton Height Commerce Park, Yeovil BA22 8UY, UK; ata.yoosefinejad@munrotechnology.com (A.Y.)
[3] Z-Prime, The Charter Building, Uxbridge, London UB8 1JG, UK; padl@zprime.ai (P.A.)
[4] Axalp Technologies AG, Louis Giroud-Strasse 26/3.OG, 4600 Olten, Switzerland; tischhauser.frederick@axalptech.com (F.T.)
* Correspondence: matthias.schaer@fhnw.ch

Abstract

Delamination is a critical failure mode in composite laminates that degrades the structural performance and load-carrying capacity. This study investigates the improvement of Mode I and Mode II interlaminar fracture toughness of carbon fiber-reinforced polymer (CFRP) laminates through the interleaving of electrospun thermoplastic nanofiber mats. Nanofiber veils were inserted between carbon fiber plies to enhance resistance to delamination under tensile opening (Mode I) and in-plane shear (Mode II) loading. The effects of nanofiber interleaving were evaluated using double cantilever beam (DCB) tests for Mode I and end notch flexure (ENF) tests for Mode II. Both tests were conducted on a symmetric quasi-isotropic laminate $[-45/45/90/0_5]_s$ containing a thick unidirectional 0° ply at the mid-plane. Thermally induced residual stresses resulting from mismatches in ply coefficients of thermal expansion and unsymmetric arm lay-ups were accounted for in the experimental determination of fracture toughness. These stresses, generated during cooling from the cure temperature, influence the effective strain energy release rate and were included in the fracture toughness calculations to ensure accurate toughness evaluation and consistency with numerical predictions. The results demonstrate improved delamination fracture toughness, highlighting the potential of nanofiber interleaving for aerospace and wind energy applications.

Keywords: carbon fiber composite laminates; Mode I fracture toughness; Mode II fracture toughness; electrospun nanofibers; interlaminar toughening; delamination resistance; thermal residual stresses; damage tolerance

Academic Editor: Constantina Lekakou

Received: 2 February 2026
Revised: 19 February 2026
Accepted: 25 February 2026
Published: 3 March 2026

1. Introduction

Continuous carbon fiber-reinforced polymer (CFRP) composite laminates are extensively utilized in aerospace, automotive, and renewable energy applications owing to their exceptional specific stiffness, high strength-to-weight ratio, and superior fatigue and corrosion resistance compared to conventional metallic materials. Despite these advantages, the inherent weakness in the through-thickness direction makes them susceptible to delamination. Delamination [1] is widely recognized as one of the most critical damage

mechanisms in composite laminates, severely compromising their structural integrity and long-term performance [2–4]. Owing to the inherently brittle and resin-rich interlayer regions, composite laminates are highly susceptible to delamination. Delamination may arise from various sources, including manufacturing defects, low-velocity impacts [4], ply-crack interactions [2], or stress concentrations near geometrical discontinuities such as holes and free edges [5]. Depending on the loading conditions, delamination can manifest in different fracture modes [6]: mode I (opening), mode II (sliding), and mode III (tearing), or as mixed-mode delamination, with each mode governing distinct propagation behaviors and energy dissipation mechanisms. While other damage mechanisms such as ply cracking [7] contribute to performance degradation, delamination is particularly detrimental because it rapidly propagates along the weak interlayer interfaces, leading to stiffness reduction, loss of load-carrying capacity, and ultimately catastrophic failure. Therefore, understanding the initiation and growth of delamination, developing strategies to enhance interlaminar toughness and improving the capability for early delamination detection prior to catastrophic growth remain critical challenges for ensuring the structural reliability and expanding the application envelope of CFRP laminates. Several studies have investigated the initiation and propagation of delamination, as well as methods for its detection; readers are referred to the following review papers for a comprehensive overview: [3,4,8–12]. The current work is focused on strategies to enhance interlaminar toughness.

Enhancing the interlaminar fracture toughness of carbon fiber-reinforced polymer laminates is critical to preventing catastrophic structural failures arising from abrupt delamination. Existing approaches for improving toughness are generally classified into resin matrix modification [13–15], Z-directional reinforcement [16], and interlayer toughening [17–20]. Among these, interlayer toughening has attracted particular interest due to its superior processability, adaptability, and compatibility with laminate design. This strategy involves inserting an interlayer between adjacent plies, where it can activate intrinsic, extrinsic, or combined toughening mechanisms depending on its molecular structure and physical characteristics. Intrinsic mechanisms improve resistance to both crack initiation and propagation, while extrinsic mechanisms mainly mitigate delamination propagation through fiber bridging, pull-out, ductile deformation, or crack deflection.

Various studies have shown that thermoplastic particles [21,22], non-woven veils [23,24], and electrospun nanofibers [25,26] can significantly alter crack propagation behavior. Nanofibrous veils have emerged as a promising class of interlayers, offering the potential to simultaneously exploit intrinsic and extrinsic mechanisms. Owing to their nanometer-scale diameters, high porosity, large specific surface area, and tunable morphology, these veils enhance energy dissipation while imposing minimal trade-offs on stiffness, strength, or thermal resistance. A review on the toughness efficiency of the veils/interleaves produced via electrospinning can be found in [27], where the effect of different veil materials and their modifications on delamination fracture toughness is studied.

This study examines the potential of commercially available electrospun thermoplastic nanofiber fleece mats (enTex and iTex by Munro Technology (Yeovil, UK)) to improve the delamination resistance of continuous-fiber HexPly® 8552 carbon/epoxy(Hexccel Corporation, Stamford, CT, USA) laminates. Four laminate configurations were investigated: a reference laminate composed exclusively of HexPly® 8552 prepreg with the lay-up $[-45/45/90/0_5]_s$, an enTex-modified laminate, and two iTex-modified laminates, named iTex NS4001 and iTex NS4401. In the modified laminates, the respective nanofiber fleece mat material (enTex or iTex) was integrated at the mid-plane of the laminate (between the middle 0° ply). The effectiveness of these modifications in enhancing interlaminar fracture toughness (G_{Ic} and G_{IIc}) was evaluated using standardized double cantilever beam (DCB) and end-notched flexure (ENF) tests, from which load–displacement curves were

obtained. In standard fracture mechanics characterization, DCB and ENF tests are commonly performed on unidirectional 0° laminates, where residual stress effects are minimal and often neglected. However, in quasi-isotropic laminates considered in this study, the presence of multiple ply orientations and unsymmetric arm lay-ups leads to non-negligible residual stress fields and bending moments that modify the effective strain energy release rate [28]. Consequently, fracture toughness values obtained from conventional data reduction methods may not accurately represent the true interlaminar behavior unless these effects are accounted for. Recognizing this limitation, the present study explicitly accounts for thermally induced residual stresses in the experimental evaluation of Mode I and Mode II fracture toughness of quasi-isotropic laminates using the method developed by Yokozeki et al. [29]. It was shown that the use of electrospun thermoplastic nanofiber fleece mats with different properties can significantly increase fracture toughness, though with differing effects on Mode I and Mode II. To better understand the effects of interlayer toughening on interface properties, the DCB and ENF experiments were also modeled in the finite element software ANSYS Mechanical (Canonsburg, PA, USA) using a combination of interface elements and the virtual crack closure technique (VCCT).

The results are discussed in detail and confirm the beneficial use of electrospun thermoplastic nanofiber fleece mats in increasing fracture toughness, as well as the important effect of thermally induced residual stresses on the fracture toughness evaluation.

2. Materials and Methods

The reference laminate was manufactured from unidirectional HexPly® 8552 carbon/epoxy prepreg. The laminate stacking sequence was a symmetric quasi-isotropic lay-up of $[-45/45/90/0_5]_s$, selected to represent a realistic structural configuration. To investigate the effect of nanofiber interleaving, the reference laminate was modified by incorporating electrospun thermoplastic nanofiber mats at the laminate mid-plane. In specimens designated as enTex, two plies of enTex nanofiber mats were embedded between the 0° plies at the mid-plane, while in specimens designated as iTex, two plies of iTex nanofiber mats were inserted at the same location. Both nanofiber materials were supplied by Munro Technology Ltd. (Yeovil, UK).

Two electrospun nonwoven systems were employed: enTex, a commercial polyamide-based nanofiber nonwoven developed to enhance interfacial interactions with the epoxy matrix and featuring a nominal thickness of approximately 20 µm, and two different versions of iTex (iTex NS4001 and iTex NS4401) with a nominal thickness of 40 µm and different modified surface chemistries to render the nanofiber systems electrically conductive. Representative scanning electron microscopy (SEM) images of the nanofiber systems are shown in Figure 1.

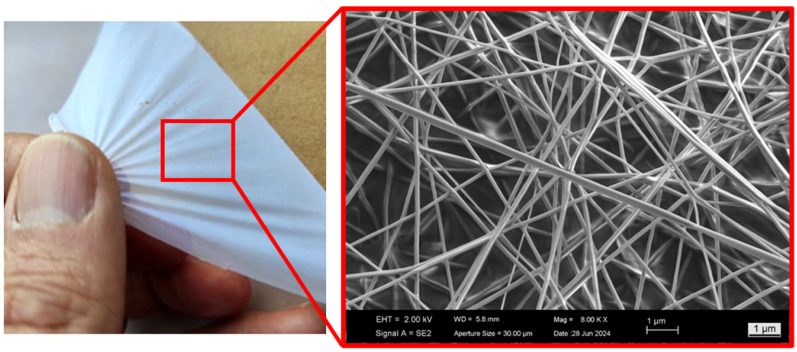

Figure 1. SEM image of the enTex nonwoven material, consisting of homogeneous polymer fibers.

Composite plates with dimensions of 270 × 270 mm were manufactured using a hot-press process following the stacking sequence shown schematically in Figure 2, which illustrates the laminate lay-up and the location of the nanofiber interleaves.

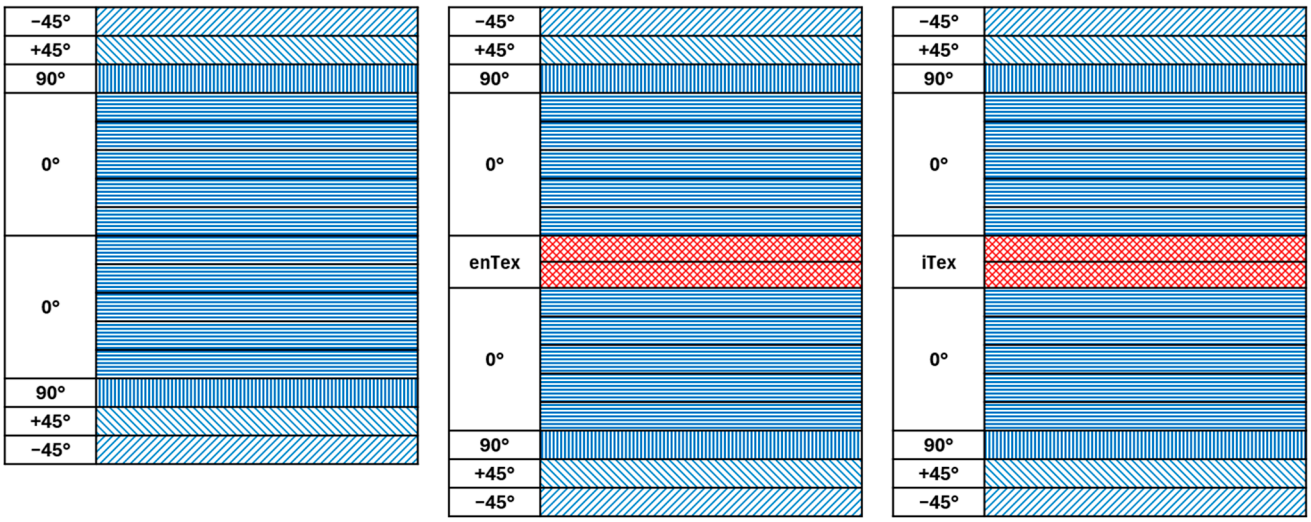

Figure 2. HexPly® 8552 prepreg reference (**left**) and two modified configurations with either enTex (**middle**) and 2 plates with iTex NS4001 or iTex NS4401 nonwoven material interleaved (**right**).

A thin polyimide (PI) film was co-cured at this interface (Figure 3) in all laminates to serve as a predefined weak layer for controlled crack initiation. After curing at 180 °C for 3 h in a closed mold and heated press (Lauffer, Horb am Neckar, Germany), the plates were cut into specimens for Mode I—DCB and Mode II—ENF testing using a Compcut 600 saw (Sharp & Tappin Technology Ltd. (Compcut), Devon, UK).

(**a**) (**b**)

Figure 3. (**a**) Lamination process of the reference configuration, in which the polyimide film inserted for crack initiation is visible, as also shown in (**b**), where this PI film within the specimen as well as the clean-cut edge of the specimens without defects can be observed.

2.1. I Double Cantilever Beam Test

According to the norm ASTM D5528-1 [30], the specimens were prepared by bonding loading blocks with dimensions of 15 mm × 15 mm × 20 mm, each containing a central 8 mm hole at the ends of the specimens. A custom bonding fixture was employed to ensure precise alignment of the blocks and uniform load introduction during testing. The sides of the specimens were coated with white paint, and laser-etched length markers were applied to facilitate accurate monitoring of crack growth. The initial delamination crack was defined using a pre-inserted polyimide film at the laminate mid-plane, which was

subsequently opened to the desired initial crack length using a razor blade. DCB tests were performed on a Zwick universal testing machine (Ulm, Germany) equipped with a 100 kN load cell, using a constant crosshead displacement rate of 1 mm/min. The test setup, including specimen geometry and loading arrangement, is shown schematically in Figure 4a, with a photograph of the actual test setup in Figure 4b. Detailed specimen dimensions are provided in Table 1.

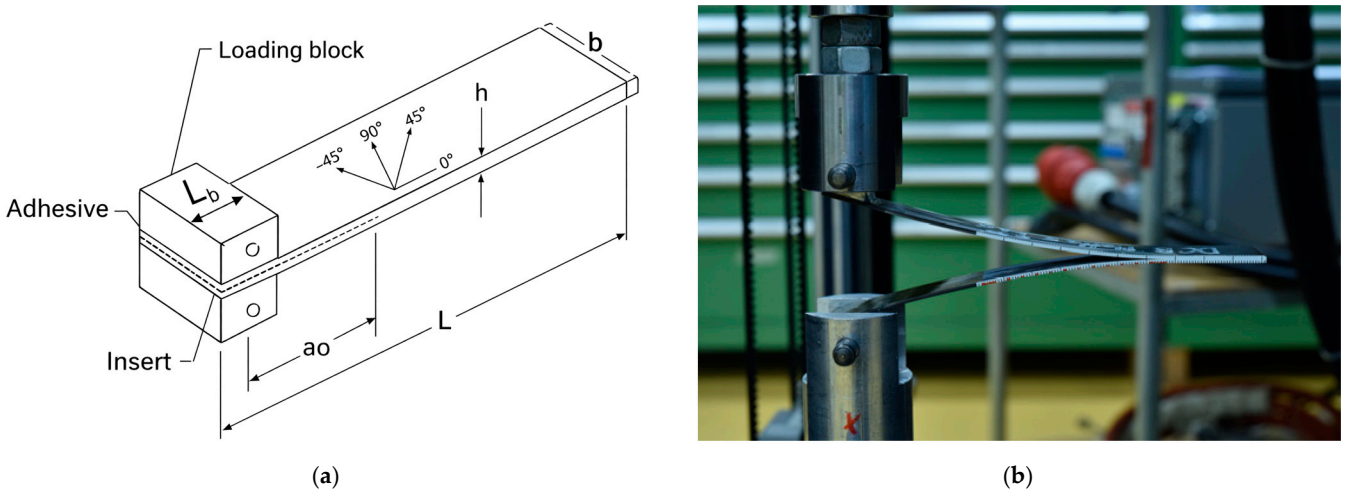

(**a**) (**b**)

Figure 4. (**a**) Schematic representation of the DCB samples used in this study, (**b**) photograph of DCB test setup.

Table 1. Dimensions of DCB samples used in this study.

Part	Symbol	Dimension	Size [mm]
DCB specimen	L	Length	150
	h	Thickness	2.7
	b	Width	20
	a_0	Precrack length	50
	L_b	Block length	15

For Mode I fracture toughness evaluation, the strain energy release rate G_{Ic} can be calculated following ASTM D5528-1 using the Modified Beam Theory (MBT) method, neglecting the effects of thermal residual stresses. The applied equation is given below:

$$G_{Ic} = \frac{3 \times P \times \delta}{2 \times b \times a_0}, \quad (1)$$

where P is the measured maximum applied load before crack growth, δ is the total crosshead displacement at load P, while the other parameters are defined in Table 1.

2.2. End-Notched Flexure Tests

According to the norm, ASTM D7905 End-Notched Flexure specimens were cut from the same 270 × 270 mm composite plates used for the preparation of the DCB specimens. Similar to the DCB specimens, the side surfaces were coated with white paint, and laser-engraved length markers were applied to facilitate crack growth monitoring. The initial delamination crack was defined using a polyimide film inserted at the laminate mid-plane during lay-up and was subsequently extended to the required initial crack length using a razor blade.

ENF tests were performed on a Zwick KN100 (Ulm, Germany) universal testing machine equipped with a 100 kN load cell. Loading was applied under three-point bending

at a constant crosshead displacement rate of 1 mm/min to ensure controlled shear-mode loading. The ENF test setup, including specimen geometry and loading configuration, is shown in Figure 5, while detailed specimen dimensions are provided in Table 2.

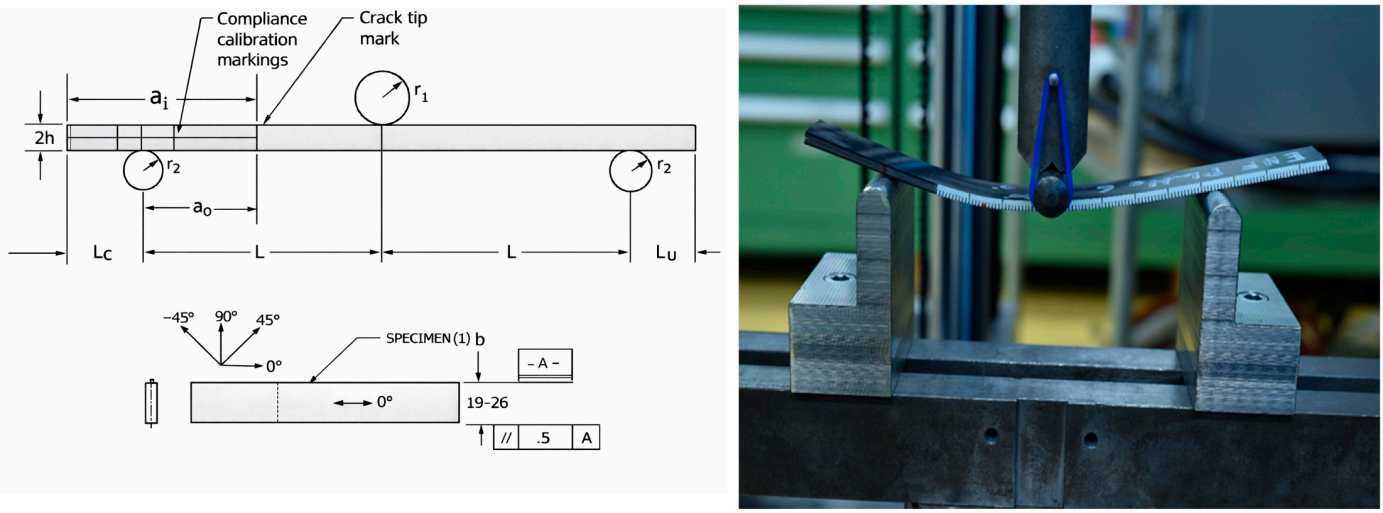

(**a**) (**b**)

Figure 5. (**a**) Schematic representation of the ENF samples used in this study, (**b**) photograph of ENF test setup.

Table 2. Dimensions of ENF samples used in this study.

Part	Symbol	Dimension	Size [mm]
ENF specimen	L	Length	50
	L_c	Length after contact point	25
	2h	Thickness	2.7
	b	Width	20
	a_0	Precrack length from contact point	30
	a_i	Precrack length total	55
	L_b	Block length	15

The Mode II interlaminar fracture toughness G_{IIc} was calculated using the standard compliance method for the ENF configuration. The applied equation is given below [31]:

$$G_{IIc} = \frac{9 \times P^2 \times {a_0}^2 \times C_b}{2 \times b \times (2L^3 + 3{a_0}^3)}, \quad (2)$$

where C_b is the so-called compliance and can be calculated from the measured material properties and geometric parameters using a linear regression according to ASTM D7905 [31].

2.3. Corrections for the Effects of Thermal Residual Stresses

In laminated composite structures, thermally induced residual stresses inevitably develop during cooling from the cure temperature as a result of mismatches in the coefficients of thermal expansion among plies with different fiber orientations. These residual stresses modify the local stress state at ply interfaces and can significantly influence both the initiation and propagation of delamination. In quasi-isotropic laminates such as those considered in the present study, the coexistence of multiple ply orientations combined with unsymmetric arm lay-ups in DCB and ENF specimens gives rise to non-negligible residual

stress fields and associated bending moments. These effects alter the effective strain energy release rate at the delamination front. As a consequence, fracture toughness values derived using conventional data reduction methods, which typically neglect residual stresses, may not accurately reflect the true interlaminar fracture behavior unless these contributions are explicitly accounted for. The present study adopts the approach of Yokozeki et al. [29], which extends Nairn's formulation [32] to include residual stresses in the calculation of energy release rates for multilayered DCB, ENF, and mixed-mode bending specimens. Using this method, the difference between the apparent fracture toughness, obtained when residual stresses are neglected (Equations (1) and (2)), and the true fracture toughness can be determined for a given laminate configuration and specimen geometry. To derive the required correction method, it has been discussed [32,33] that for materials subjected to only traction-prescribed boundaries (including temperature changes), the energy release rate can be expressed as

$$G = \frac{\mathrm{d}}{\mathrm{d}A}\left(\frac{1}{2}\int_{S_T} \widetilde{\mathbf{T}} \cdot \mathbf{u}^m \mathrm{d}S + \int_{S_T} \widetilde{\mathbf{T}} \cdot \mathbf{u}^r \mathrm{d}S + \frac{1}{2}\int_{S_T} \boldsymbol{\sigma}^r \cdot \boldsymbol{\alpha}\, \Delta T\, \mathrm{d}V\right), \tag{3}$$

where $\boldsymbol{\sigma}^r$, $\boldsymbol{\alpha}$, $\mathbf{u}$ and $\widetilde{\mathrm{T}}$ denote, respectively, the stress tensor, coefficient of thermal expansion (CTE) tensor, displacement vector, and traction vector prescribed in traction boundary conditions. Additionally, A is the fracture area, V is the volume of the material, S_T is the area on which traction is prescribed, and ΔT is the uniform temperature difference defined by $\Delta T = T - T_0$, where T is the current temperature and T_0 is the reference temperature for which the strains and stresses are zero with no internal or imposed external stresses.

Nairn [32] applied the general form of the energy release rate introduced in Equation (3) to a multilayered beam, as shown in Figure 6.

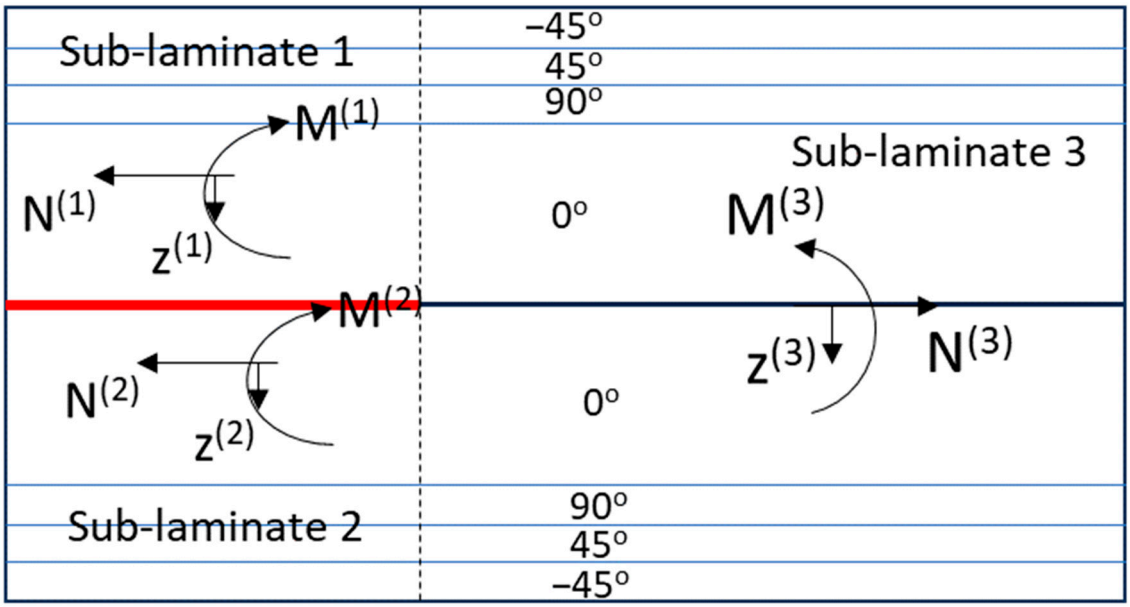

Figure 6. Schematic of sub-laminates in DCB and ENF tests for calculation of the effects of thermal residual stresses.

In the beam model, each sub-laminate (cracked arms 1 and 2, and the intact beam 3) is modeled as an equivalent homogeneous beam incorporating residual thermal stresses, and it satisfies the following constitutive relation:

$$\begin{Bmatrix} N^{(k)} \\ M^{(k)} \end{Bmatrix} = \begin{bmatrix} A_{11}^{(k)} & B_{11}^{(k)} \\ B_{11}^{(k)} & D_{11}^{(k)} \end{bmatrix} \begin{Bmatrix} \varepsilon_0^{(k)} \\ \kappa^{(k)} \end{Bmatrix} - \begin{Bmatrix} N_T^{(k)} \\ M_T^{(k)} \end{Bmatrix} \Delta T, \tag{4}$$

or in its inverse form

$$\begin{Bmatrix} \varepsilon_0^{(k)} \\ \kappa^{(k)} \end{Bmatrix} = \begin{bmatrix} C_\varepsilon^{(k)} & C_{\varepsilon\kappa}^{(k)} \\ C_{\varepsilon\kappa}^{(k)} & C_\kappa^{(k)} \end{bmatrix} \begin{Bmatrix} N^{(k)} \\ M^{(k)} \end{Bmatrix} + \begin{Bmatrix} \alpha_\varepsilon^{(k)} \\ \alpha_\kappa^{(k)} \end{Bmatrix} \Delta T, \tag{5}$$

where

$$\begin{aligned} A_{11}^{(k)} &= b\sum_i E_i^{(k)} \left(z_i^{(k)} - z_{i-1}^{(k)} \right), \\ B_{11}^{(k)} &= \frac{1}{2} b\sum_i E_i^{(k)} \left(z_i^{(k)2} - z_{i-1}^{(k)2} \right), \\ D_{11}^{(k)} &= \frac{1}{3} b\sum_i E_i^{(k)} \left(z_i^{(k)3} - z_{i-1}^{(k)3} \right), \\ N_T^{(k)} &= b\sum_i E_i^{(k)} \alpha_i^{(k)} \left(z_i^{(k)} - z_{i-1}^{(k)} \right), \\ M_T^{(k)} &= \frac{1}{2} b\sum_i E_i^{(k)} \alpha_i^{(k)} \left(z_i^{(k)2} - z_{i-1}^{(k)2} \right), \end{aligned} \tag{6}$$

and

$$\begin{aligned} C_\varepsilon^{(k)} &= \frac{D_{11}^{(k)}}{A_{11}^{(k)} D_{11}^{(k)} - B_{11}^{(k)2}}, \\ C_{\varepsilon\kappa}^{(k)} &= \frac{-B_{11}^{(k)}}{A_{11}^{(k)} D_{11}^{(k)} - B_{11}^{(k)2}}, \\ C_\kappa^{(k)} &= \frac{A_{11}^{(k)}}{A_{11}^{(k)} D_{11}^{(k)} - B_{11}^{(k)2}}, \\ \alpha_\varepsilon^{(k)} &= \frac{D_{11}^{(k)} N_T^{(k)} - B_{11}^{(k)} M_T^{(k)}}{A_{11}^{(k)} D_{11}^{(k)} - B_{11}^{(k)2}}, \\ \alpha_\kappa^{(k)} &= \frac{A_{11}^{(k)} M_T^{(k)} - B_{11}^{(k)} N_T^{(k)}}{A_{11}^{(k)} D_{11}^{(k)} - B_{11}^{(k)2}}, \end{aligned} \tag{7}$$

In the above equations, $N^{(k)}$ and $M^{(k)}$ are the resultant force and bending moment, $E^{(k)}$ and $\alpha^{(k)}$ are, respectively, the axial Young's modulus and thermal expansion coefficient in the axial direction, $z^{(k)}$ is the position from the mid-plane in sub-laminate (k), b is the width of the sample and the subscript (i) denotes each layer in each sub-laminate.

Finally, the general form of the energy release rate in a cracked laminate with residual stresses is given as follows [32], corresponding to Figure 6, where the positive directions of the resultant forces and moments are defined.

$$\begin{aligned} G = \frac{1}{2b} & \begin{pmatrix} C_\kappa^{(1)} M^{(1)2} + C_\kappa^{(2)} M^{(2)2} - C_\kappa^{(3)} M^{(3)2} \\ + C_\varepsilon^{(1)} N^{(1)2} + C_\varepsilon^{(2)} N^{(2)2} - C_\varepsilon^{(3)} N^{(3)2} \\ + 2C_{\varepsilon\kappa}^{(1)} M^{(1)} N^{(1)} + 2C_{\varepsilon\kappa}^{(2)} M^{(2)} N^{(2)} \\ - 2C_{\varepsilon\kappa}^{(3)} M^{(3)} N^{(3)} \end{pmatrix}, \\ + \frac{\Delta T}{b} & \begin{pmatrix} \alpha_\kappa^{(1)} M^{(1)} + \alpha_\kappa^{(2)} M^{(2)} - \alpha_\kappa^{(3)} M^{(3)} \\ + \alpha_\varepsilon^{(1)} N^{(1)} + \alpha_\varepsilon^{(2)} N^{(2)} - \alpha_\varepsilon^{(3)} N^{(3)} \end{pmatrix} \\ + \frac{(\Delta T)^2}{2b} & \left(I^{(1)} + I^{(2)} - I^{(3)} \right). \end{aligned} \tag{8}$$

where the last terms in Equation (8) are defined as follows:

$$I^{(k)} = N_T^{(k)} \alpha_\varepsilon^{(k)} + M_T^{(k)} \alpha_\kappa^{(k)} - b\sum_i E_i^{(k)} \alpha_i^{(k)2} t_i^{(k)}, \tag{9}$$

and where $t_i^{(k)}$ is the thickness of the *i*th ply in the (*k*) sub-laminate.

It should be noted that Equation (8) is applicable to both DCB and ENF specimens. However, geometric nonlinearities, in-plane transverse deformations, and out-of-plane normal and shear deformations are neglected in the present formulation, as the analysis is based on a beam representation within the framework of classical laminate theory.

Considering a DCB specimen (Figure 4a), the energy release rate is obtained using Equation (8). Contact between the cracked arms is neglected, since the arms separate during loading in standard DCB configurations. However, such contact effects can be accounted for using the original formulation proposed by Nairn [32]. In the DCB test, the loading conditions near the crack tip are described as follows [29]:

$$\begin{array}{l} For\ DCB: \\ M^{(1)} = Pa_0,\ \ M^{(2)} = -Pa_0,\ \ M^{(3)} = 0,\ , \\ N^{(1)} = 0,\ \ N^{(2)} = 0,\ \ N^{(3)} = 0. \end{array} \tag{10}$$

where a_0 is the crack length. By substituting Equation (10) into Equation (8), the energy release rate for the DCB specimen in the presence of residual stresses is obtained as follows:

$$\begin{array}{l} G_{DCB} = \frac{P^2}{2b}\left(C_\kappa^{(1)} + C_\kappa^{(2)}\right)a_0^2 + \frac{P\Delta T}{b}\left(\alpha_\kappa^{(1)} - \alpha_\kappa^{(2)}\right)a_0 \\ \quad + \frac{(\Delta T)^2}{2b}\left(I^{(1)} + I^{(2)} - I^{(3)}\right). \end{array} \tag{11}$$

The first term of Equation (11) represents the energy release rate associated solely with mechanical loading. Since classical beam theory neglects shear deformation and thickness-direction extensional effects, the actual crack length should be replaced by an equivalent crack length. Accordingly, the first term requires modification through the introduction of an end-correction parameter for each cracked arm. In contrast, the induced deformations arising from distributed bending moments due exclusively to temperature changes are adequately captured within the present formulation; therefore, the second and third terms of Equation (11) are considered reliable. In practice, standard procedures recommend the use of the experimental compliance method to evaluate the interfacial fracture toughness associated with mechanical loading (i.e., the apparent fracture toughness). Moreover, the determination of accurate end-correction parameters for general layered configurations remains uncertain. For these reasons, the first term of Equation (11) is not evaluated numerically in the present study but is instead obtained experimentally from the DCB tests. Using the experimentally obtained apparent fracture toughness G_{DCB}^{Exp}, the true fracture toughness can be calculated as

$$G_{DCB} = G_{DCB}^{Exp} + \frac{P\Delta T}{b}\left(\alpha_\kappa^{(1)} - \alpha_\kappa^{(2)}\right)a_0 + \frac{(\Delta T)^2}{2b}\left(I^{(1)} + I^{(2)} - I^{(3)}\right), \tag{12}$$

Equation (12) indicates that the true energy release rates can be calculated from the apparent energy release rates (considering only mechanical loading), together with the constants of the layered specimen (e.g., mechanical properties and specimen geometry), as well as the crack length, applied load, and temperature change.

In the case of the ENF test, the loading condition near the crack tip can be described as [29]

$$\begin{array}{l} For\ ENF: \\ M^{(1)} = 0,\ \ M^{(2)} = \frac{P}{2}a_0,\ \ M^{(3)} = \frac{P}{2}a_0, \\ N^{(1)} = 0,\ \ N^{(2)} = 0,\ \ N^{(3)} = 0 \end{array} \tag{13}$$

By substituting Equation (13) into Equation (8), the energy release rate for the ENF specimen, accounting for residual stresses, is obtained as follows:

$$G_{ENF} = \frac{P^2}{8b}\left(C_\kappa^{(2)} - C_\kappa^{(3)}\right)a_0^2 + \frac{P\Delta T}{2b}\left(\alpha_\kappa^{(2)} - \alpha_\kappa^{(3)}\right)a_0 + \frac{(\Delta T)^2}{2b}\left(I^{(1)} + I^{(2)} - I^{(3)}\right). \quad (14)$$

Similar to DCB specimens, the first term of Equation (14) is corrected using an equivalent crack length. The apparent energy release rate (or apparent toughness) is then determined via the experimental compliance method, yielding the following form of Equation (14):

$$G_{ENF} = G_{ENF}^{Exp} + \frac{P\Delta T}{2b}\left(\alpha_\kappa^{(2)} - \alpha_\kappa^{(3)}\right)a_0 + \frac{(\Delta T)^2}{2b}\left(I^{(1)} + I^{(2)} - I^{(3)}\right). \quad (15)$$

The true energy release rates can be determined from the apparent energy release rates and the constants of the layered specimens. The procedure for experimentally obtaining the apparent fracture toughness is described above in Equations (1) and (2).

2.4. Finite Element Modeling of DCB and ENF Specimens

To complement the experimental characterization of Mode I and Mode II delamination, finite element models of both test configurations were developed in ANSYS Mechanical R2024 (Canonsburg, PA, USA). The primary objective of these simulations was to reproduce the load–displacement responses of the DCB and ENF specimens, with a particular emphasis on capturing the initial deviation from linear behavior associated with the onset of crack propagation. By assuming different values of critical fracture toughness, the corresponding energy release rates during delamination growth were evaluated and subsequently compared with the experimentally determined values. The modeling approach is based on linear elastic laminate behavior with explicit representation of the delamination surface by interface elements and using the virtual crack closure technique (VCCT) as a fracture mechanics approach.

Geometry and Mesh

Three-dimensional finite element models of the DCB and ENF specimens were developed using the exact specimen geometries, consistent with the experimental configurations shown in Figures 4a and 5a and the dimensions summarized in Tables 1 and 2. The composite laminates were discretized using solid continuum elements, while a predefined delamination path was explicitly introduced at the laminate mid-plane through the use of interface elements. The composite plies were modeled using three-dimensional linear hexahedral solid elements (SOLID185). These elements were selected to provide an efficient and stable representation of the orthotropic elastic behavior of the composite laminate while accurately capturing bending and shear deformations along the specimen length and through the thickness. The use of linear solid elements ensured numerical robustness and compatibility with the interface element formulation adopted for fracture analysis. Higher-order solid elements (e.g., SOLID186 or SOLID187) were not employed in the present study, as the VCCT-based delamination analysis in ANSYS is most robust when paired with linear solid elements and matching nodal connectivity at the crack interface. In addition, mesh refinement in the vicinity of the crack front was used to compensate for the lower-order interpolation and to ensure convergence of the strain energy release rate calculations. Crack initiation and propagation were modeled by introducing zero-thickness interface elements (INTER205) along the predefined mid-plane delamination surface. These interface elements enable the direct evaluation of Mode I and Mode II energy release rates using the virtual crack closure technique (VCCT). To ensure accurate VCCT calculations, the

interface elements were arranged such that nodes on the upper and lower crack faces were aligned in a one-to-one correspondence, satisfying the kinematic requirements of the VCCT formulation. This approach allows the strain energy released during incremental crack extension to be computed directly from nodal forces and relative displacements ahead of and behind the crack front. Local contact interactions arising during specimen deformation were accounted for using contact elements (CONTA174) where necessary, ensuring realistic load transfer and preventing numerical interpenetration. Meshing was performed using a structured grid along both the thickness and length directions to improve accuracy. A mesh convergence study was carried out by progressively increasing the number of elements through the thickness and refining the mesh in the vicinity of the delamination path, while monitoring the effect on the load–displacement response. It was found that using three elements through the thickness and a square element size of 3 mm along the length and width of the specimen was sufficient to achieve converged results. Convergence was considered adequate when further mesh refinement led to changes of less than approximately 1% in the calculated maximum load on the load–displacement curve.

The composite lamina (HexPly® 8552) was modeled as an orthotropic linear elastic material with properties from a manufacturer data sheet [34], as in Table 3.

Table 3. Unidirectional ply properties for HexPly® 8552 [34], where transverse isotropy is assumed.

Property	Symbol	Value
Axial Young's modulus	E_{11}	134 GPa
Transverse Young's modulus	$E_{22} = E_{33}$	10 GPa
In-plane Poisson's ratio	$\upsilon_{12} = \upsilon_{13}$	0.27
Out-of-plane Poisson's ratio	υ_{23}	0.4
In-plane shear modulus	$G_{12} = G_{13}$	3.5 GPa
Out-of-plane shear modulus	G_{23}	3.57 GPa
Axial thermal expansion coefficient	α_{11}	$0.21 \times 10^{-6\circ}$/C
Transverse thermal expansion coefficient	$\alpha_{22} = \alpha_{33}$	$33.3 \times 10^{-6\circ}$/C
Ply thickness	t_{ply}	0.166 mm

For the delamination interface elements, the VCCT formulation requires the specification of critical energy release rates, which were assigned based on experimentally determined fracture toughness values. In VCCT, the energy required to extend the crack by a small amount is computed from the reaction forces and corresponding displacements ahead of and behind the crack tip. Boundary conditions in the DCB model mirrored the experimental setup, and for both DCB and ENF specimens, loading was applied as a prescribed displacement. To account for thermally induced residual stresses, an additional analysis step was included, in which the specimens were uniformly cooled from the curing temperature to room temperature ($\Delta T = -155\ ^\circ C$) prior to the application of mechanical loading in both DCB and ENF models. All simulations were performed using the implicit static structural solver in ANSYS Mechanical R2024. Nonlinear geometric effects were included where appropriate to account for large displacements during crack propagation. The numerical load–displacement responses were then compared with experimentally measured curves. The influence of the electrospun nanofiber mats was incorporated by

assigning higher fracture toughness values at the mid-plane interface, while their actual ply thickness was neglected due to their negligible contribution to the overall laminate geometry.

3. Results and Discussion

In this first part, we will present the results of the reference configuration compared to the modification with enTex and iTex NS4001 and iTex NS4401. In the second part, the experimentally obtained data is compare with the simulated test, including aspects with and without residual stresses.

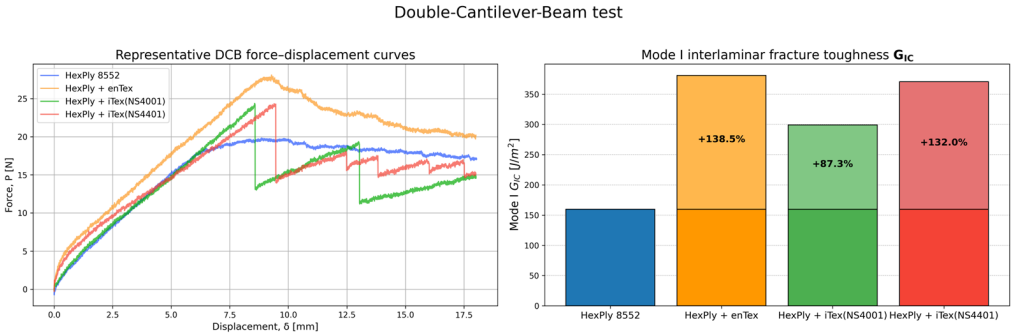

Figure 7. Results' load–displacement curves of the DCB.

For Mode I G_{Ic}, the following results were obtained: The baseline material HexPly® 8552 exhibited an average value of approximately 160 J/m^2. With the integration of enTex, G_{Ic} increased by +138.5%. With iTex NS4001, an increase of +87.3% was achieved, and with iTex NS4401, an increase of +132.0% was achieved, as can be observed in Figure 7.

In Figure 8, the representative load–displacement curves of the ENF specimens exhibit a generally similar trend across all configurations. However, it was clearly observed that the specimens with iTex NS4001 nonwoven material sustained the highest load levels up to failure. This indicates an increased resistance to shear-dominated loading and an improved delamination resistance.

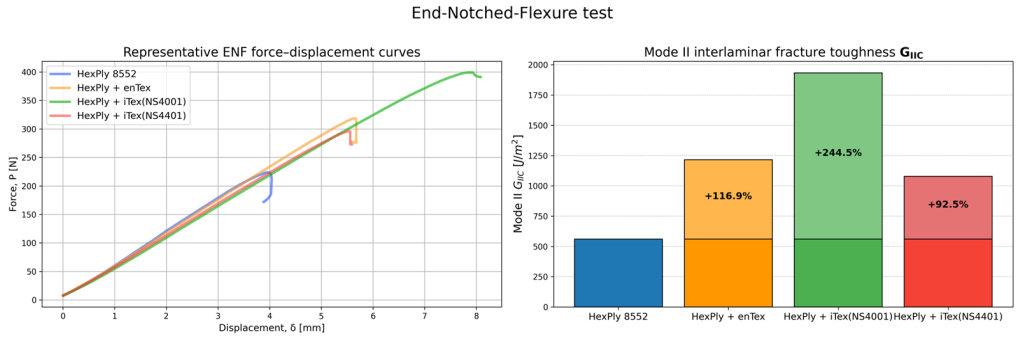

Figure 8. Results' load–displacement curves of the ENF.

It is particularly noteworthy that ENF tests revealed an increase in G_{IIc} of +116.9% (enTex), +244.5% (iTex NS4001) and +92.5% (iTex NS4401), indicating a significantly enhanced resistance to delamination and, consequently, improved damage tolerance under impact loading conditions.

Figures 9 and 10 show box-and-whisker plots of the measured fracture toughness obtained from Double Cantilever Beam and End-Notched Flexure tests, respectively. Figure 9 presents the Mode I fracture toughness G_{IC}, calculated using Equation (1), while Figure 10 shows the Mode II fracture toughness G_{IIC}, calculated using Equation (2). In both cases, the fracture toughness values were determined from the force and displacement at the

peak load, together with the initial crack length and specimen width. Owing to the specific laminate configuration, pronounced thermal residual stresses are present in the laminates, which promote crack opening within the material. In particular, for the DCB specimens, it was observed that, in the unloaded initial state, the specimen arms did not fully close and had to be pressed together against the residual stresses. Therefore, for each material system, the fracture toughness values modified to account for thermal residual stresses are also shown, calculated using Equation (3) for the DCB tests and Equation (4) for the ENF tests. In each box-and-whisker plot, the box represents the interquartile range, the horizontal line denotes the median, the whiskers indicate the data spread, and the markers indicate individual test results and mean values.

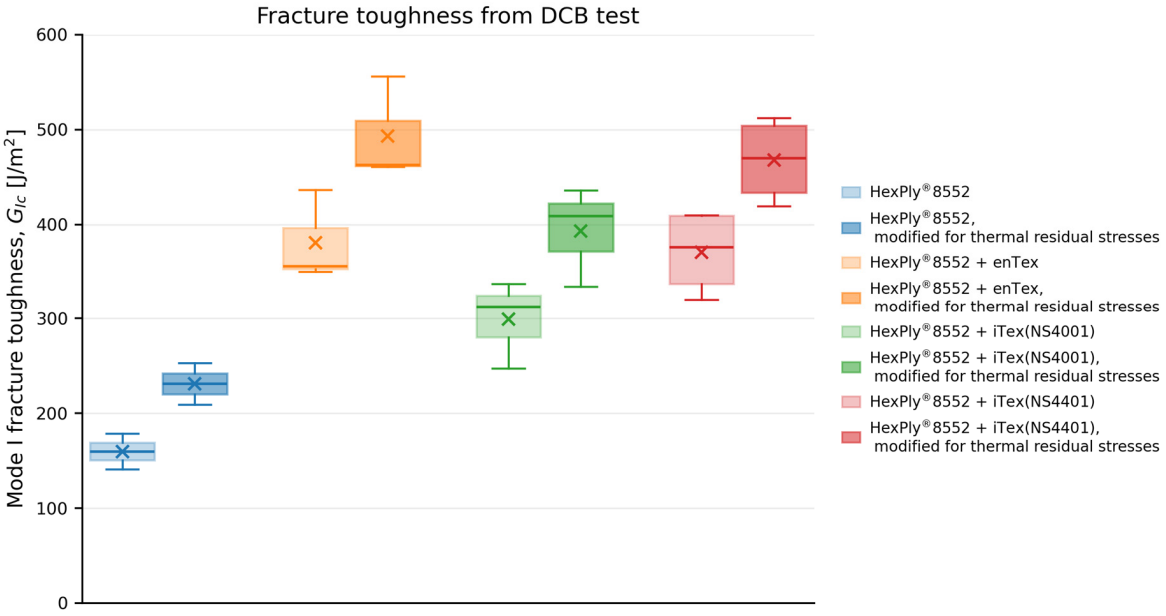

Figure 9. Measured G_{Ic} from DCB test for different samples with and without considering the effects of thermal residual stresses.

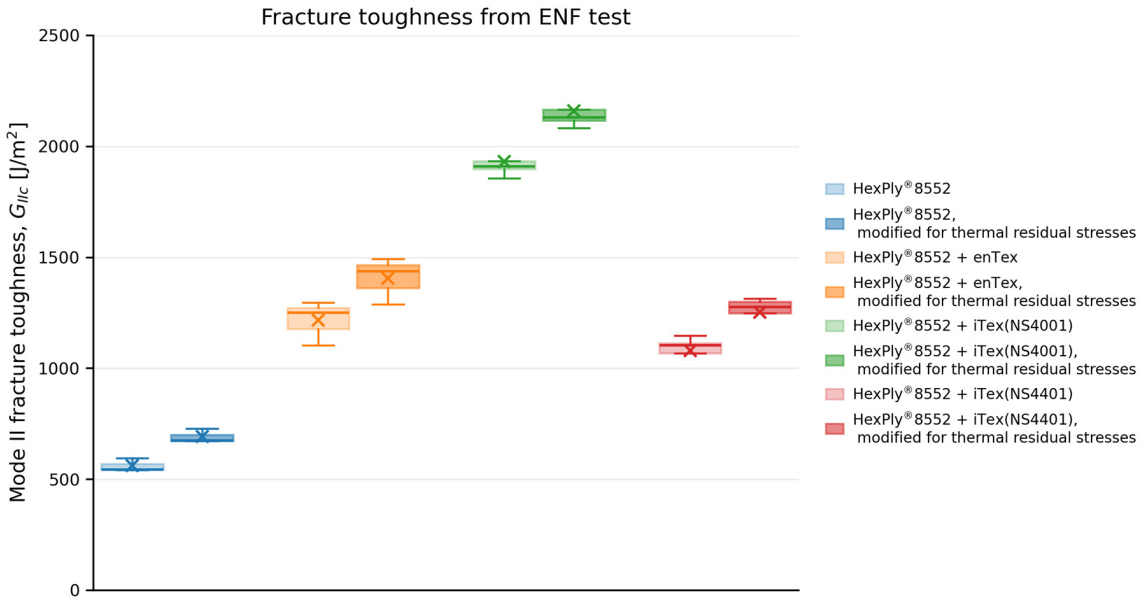

Figure 10. Measured G_{IIc} from ENF test for different samples with and without considering the effects of thermal residual stresses.

It can be seen in Figures 9 and 10 that the introduction of thermoplastic interleaves significantly increases both Mode I and Mode II fracture toughness compared to the baseline HexPly® 8552 laminate. For both DCB and ENF tests, laminates modified with enTex and iTex exhibit substantially higher fracture toughness values, indicating enhanced resistance to crack initiation and propagation. In all material systems, the fracture toughness values corrected for thermal residual stresses are consistently higher than the corresponding unmodified values, highlighting the contribution of residual stresses to crack opening and energy dissipation.

Furthermore, the iTex system with NS4001 exhibits the highest fracture toughness in ENF tests, whereas the NS4401-based system shows comparatively lower, though still enhanced, toughness. This trend is consistent across both fracture modes, suggesting that the chemical nature and morphology of the interleaf material play a critical role in governing interlaminar fracture behavior. The primary distinction between the two iTex grades, which share a common base polymer, lies in the inter-fiber pore size distribution and overall morphology governed by their respective additive packages. Specifically, the additives in NS4401 yield a structure with reduced resin permeability and a slightly greater thickness (approximately 35 microns) compared to the NS4001 grade. Overall, the combined results from Figures 9 and 10 indicate that both the choice of interleaf system and the consideration of thermal residual stresses are essential for accurately assessing and optimizing interlaminar fracture toughness under Mode I and Mode II loading conditions.

As shown in Figure 9, accounting for thermal residual stresses increases the apparent fracture toughness obtained from DCB tests by an average of 94 J/m^2 for the quasi-isotropic laminate considered, using the formulation provided in Equation (12). This represents a significant correction relative to the experimental values, emphasizing that the effect of thermal residual stresses cannot be neglected.

Similarly, as illustrated in Figure 10 and using Equation (15), the Mode II fracture toughness obtained from ENF tests must be increased by an average of 180 J/m^2 to account for the presence of thermal residual stresses in the laminate. These results quantitatively demonstrate the substantial influence of thermal residual stresses on the experimentally measured fracture toughness and underline the necessity of including this correction when interpreting DCB and ENF test results.

The significant enhancements in both Mode I and Mode II fracture toughness observed with the integration of enTex and iTex veils can be attributed to several synergistic toughening mechanisms inherent to thermoplastic interleaving. In Mode I (DCB), the presence of nonwoven fibers likely promotes crack-path deflection and micro-bridging, forcing the crack to navigate a more tortuous path around the thermoplastic fibers rather than propagating linearly through the brittle epoxy matrix. Additionally, localized plastic deformation of the thermoplastic filaments during crack opening absorbs a substantial amount of energy, consistent with previous reports on electrospun veils.

In Mode II (ENF), the superior performance of the iTex NS4001 grade indicates that its specific fiber morphology and distribution optimize the interlaminar shear resistance. The thermoplastic veils function as a compliant interlayer that effectively redistributes shear stresses and inhibits the formation of cusps or micro-cracks ahead of the main crack tip. These mechanisms collectively enhance energy dissipation during crack propagation, contributing to the observed increases in apparent fracture toughness.

While these mechanical trends strongly suggest the involvement of fiber bridging, plastic voiding, and fiber pull-out, a definitive confirmation of these mechanisms requires detailed microscopic analysis. Future work, including scanning electron microscopy (SEM) of the fracture surfaces, is needed to characterize the fiber–matrix interface and directly

visualize the specific energy dissipation mechanisms that distinguish the baseline laminates from the interleaved configurations.

A comparison of Figures 9 and 10 shows that the scatter is generally lower in the ENF (Mode II) tests than in the DCB (Mode I) tests, as evidenced by the narrower interquartile ranges and shorter whiskers in the box-and-whisker plots for most material systems. This trend is observed for both the unmodified fracture toughness values and those corrected for thermal residual stresses. The lower scatter in the ENF results can be attributed to the more stable and controlled crack propagation under shear-dominated (Mode II) loading, as well as the reduced sensitivity of the ENF configuration to the initial crack length, specimen alignment, and residual opening effects. In contrast, the DCB test is highly sensitive to crack opening behavior and thermal residual stresses, which can induce partial crack opening in the unloaded state and increase variability in the measured response. Consequently, Mode I fracture toughness measurements exhibit greater scatter, particularly for interleaved laminates where local variations in interleaf distribution and crack-path deflection play a more pronounced role.

Having obtained the Mode I and Mode II fracture toughness values from experiments on samples with and without thermoplastic interleaves, it is now useful to employ these values in numerical simulations to reproduce the load–displacement curves of the DCB and ENF tests. This approach provides an additional verification of the experimental results and demonstrates how the effects of thermoplastic interleaves can be incorporated into simulations. It also enables the assessment of the significant influence of thermal residual stresses, since accounting for these stresses has substantially increased the measured fracture toughness values.

Figures 11–14 present the experimentally measured load–displacement responses of the four different plates, both with and without thermoplastic interleaves in the DCB test. Alongside the experimental data, numerical predictions are shown, assuming different values of Mode I fracture toughness, which include the effects of thermal residual stresses. In each figure, numerical results corresponding to a range of fracture toughness values are provided, consistent with those measured and reported in Figure 9 for each plate. The scatter in the experimental results arising from repeated tests on different specimens is also illustrated.

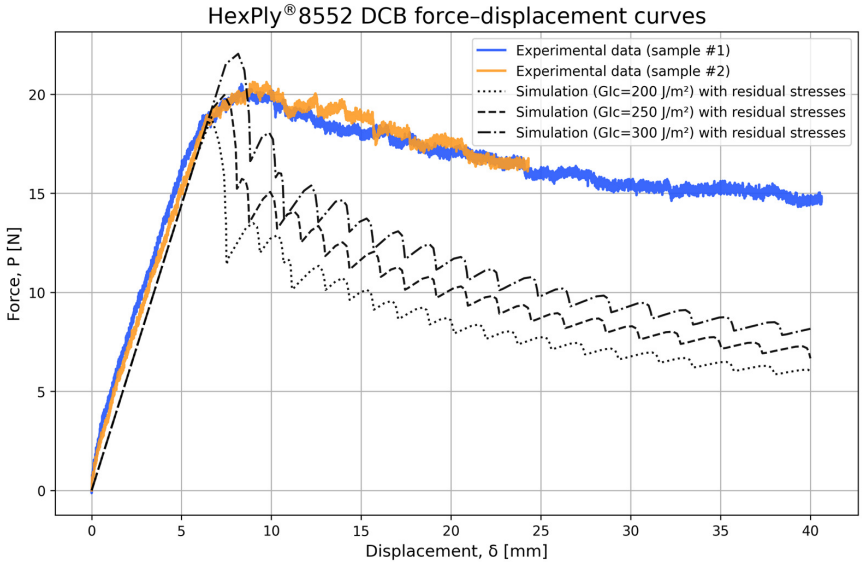

Figure 11. Experimental and numerical load–displacement curve from DCB test for samples without thermoplastic interleaves.

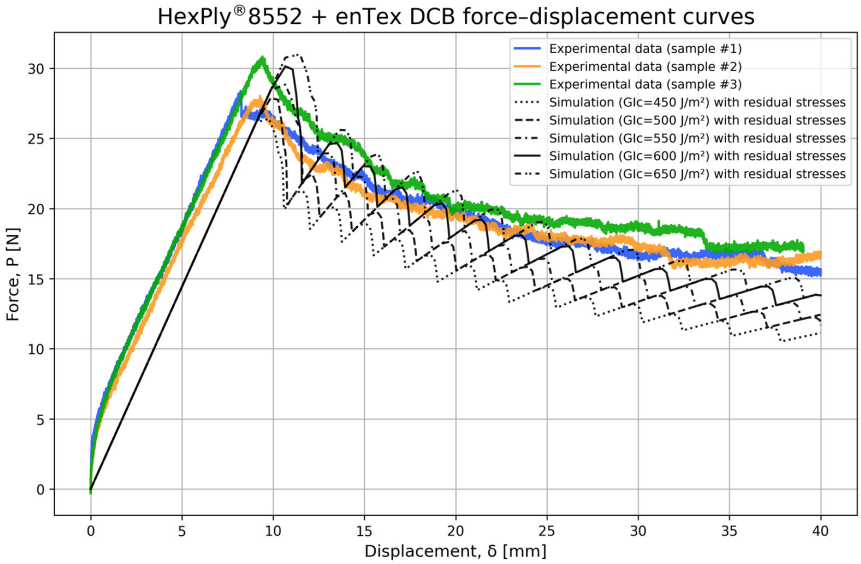

Figure 12. Experimental and numerical load–displacement curve from DCB test for samples with enTex as thermoplastic interleaves.

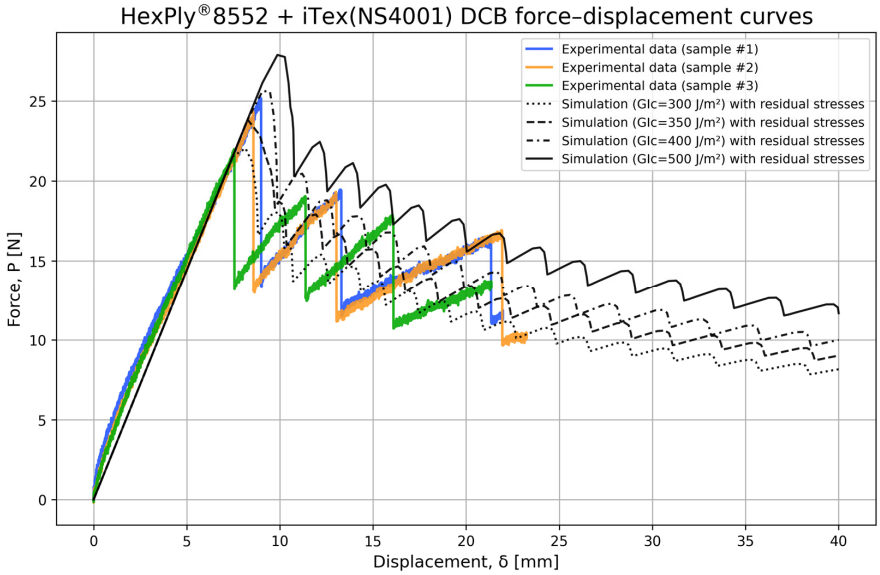

Figure 13. Experimental and numerical load–displacement curve from DCB test for samples with iTex (NS4001) as thermoplastic interleaves.

A general observation from Figures 11–14 is that the numerical model accurately predicts the first deviation from linear behavior, the peak load, and thus the onset of crack propagation when a Mode I fracture toughness consistent with experimental measurements, including the effects of thermal residual stresses, is assumed. This increases confidence in both the measured Mode I fracture toughness and the corrections applied to account for thermal residual stresses. In addition, the initial stiffness of the samples is well predicted, indicating that the ply material properties and sample geometries, including the initial crack length, are accurately characterized. A good agreement between the numerical model and experimental results is observed beyond initial crack growth for samples with enTex and iTex interleaves (Figures 12–14). In contrast, the sample without thermoplastic interleaves (Figure 11) exhibits crack growth behavior that differs from model predictions. This discrepancy may be attributed to fiber bridging between the 0° plies at the mid-plane of the HexPly® 8552 laminate without thermoplastic interleaves. Unlike the interleaved

samples (Figures 12–14), this fiber bridging inhibits abrupt crack propagation, resulting in a more gradual crack growth, as can be observed in the experimental results of Figure 11.

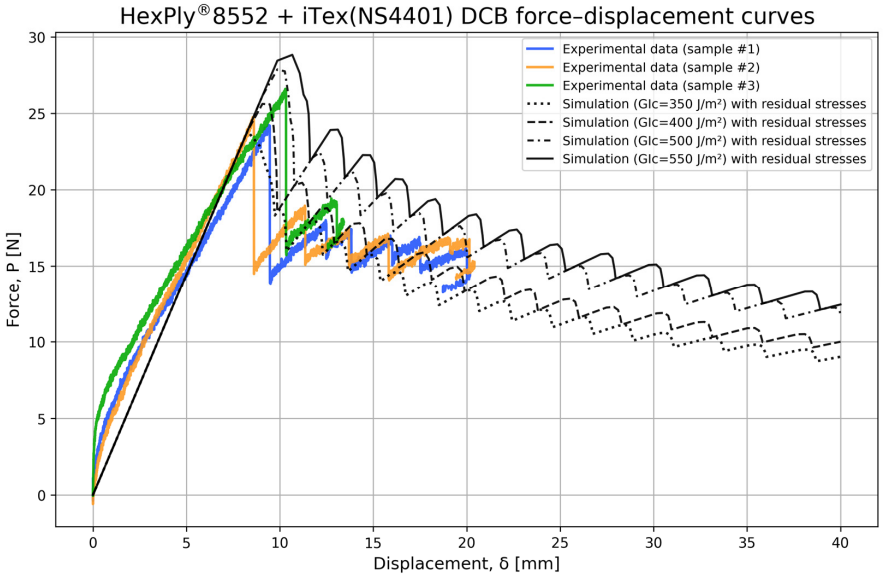

Figure 14. Experimental and numerical load–displacement curve from DCB test for samples with iTex (NS4401) as thermoplastic interleaves.

Similarly, Figures 15–18 show the experimentally obtained load–displacement curves from ENF tests performed on the four plate configurations, both with and without thermoplastic interleaves. These experimental results are compared with numerical ENF predictions calculated using different Mode II fracture toughness values that account for thermal residual stresses. For each plate, the numerical responses span a range of fracture toughness values consistent with those measured and reported in Figure 10. The variability in the experimental response, resulting from repeated tests on multiple specimens, is also included.

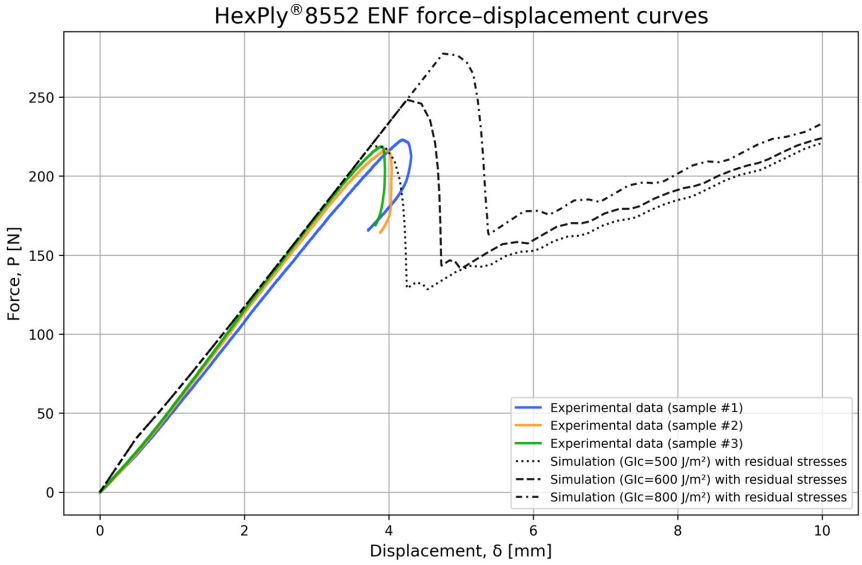

Figure 15. Experimental and numerical load–displacement curve from ENF test for samples without thermoplastic interleaves.

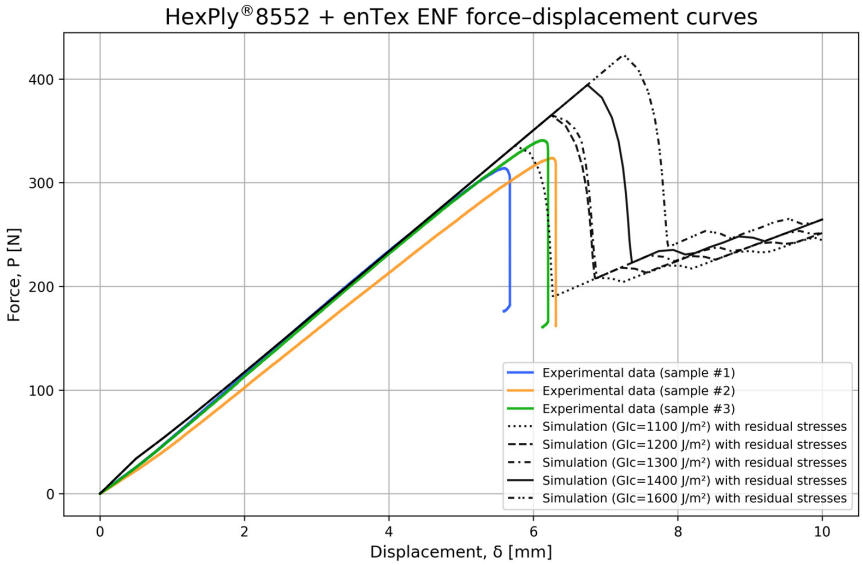

Figure 16. Experimental and numerical load–displacement curve from ENF test for samples with enTex as thermoplastic interleaves.

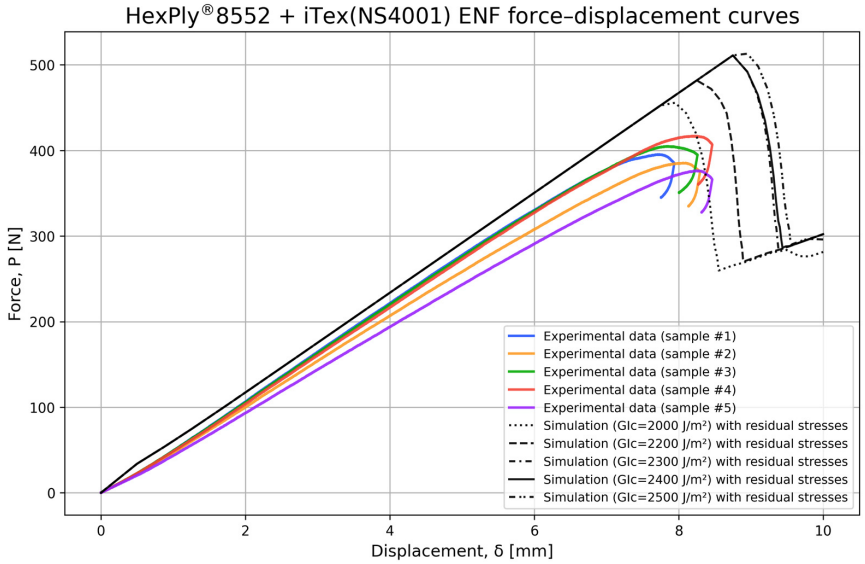

Figure 17. Experimental and numerical load–displacement curve from ENF test for samples with iTex (NS4001) as thermoplastic interleaves.

The general observations taken from the DCB tests can be similarly mentioned for the ENF results in Figures 15–18, involving rather good agreement between the modeling and experimental results, confirming the measured fracture toughness in Mode II for samples with and without thermoplastic interleaves. It can however be seen that there is a larger scatter in the experimental results for iTex samples both in terms of initial stiffness and peak load for crack initiation. However, it was clearly observed that the specimens with iTex nonwoven material sustained the highest load levels up to failure. This indicates an increased resistance to shear-dominated loading and improved delamination resistance. Numerous studies have repeatedly demonstrated that the interlaminar shear fracture toughness, G_{IIc}, is a key parameter in assessing the impact damage resistance of fiber-reinforced laminates. Nettles and Scharber [35] reported a direct correlation between G_{IIc} and the extent of impact-induced delamination, while G_I showed no significant influence on post-impact residual compressive strength. In addition, Lai et al. [36] confirmed through FEM simulations that G_{IIc} plays a dominant role in the impact resistance of laminates. Thus,

the results highlight the benefit of using iTex to improve damage tolerance, particularly under compression-after-impact loading. Recent studies corroborate the strong Mode I gains observed with electrospun veils, attributed primarily to plastic deformation within the interleaf. For instance, Palazzetti et al. [37] reported substantial G_{Ic} increases with nylon 6,6 veils, which align with the observation in this paper.

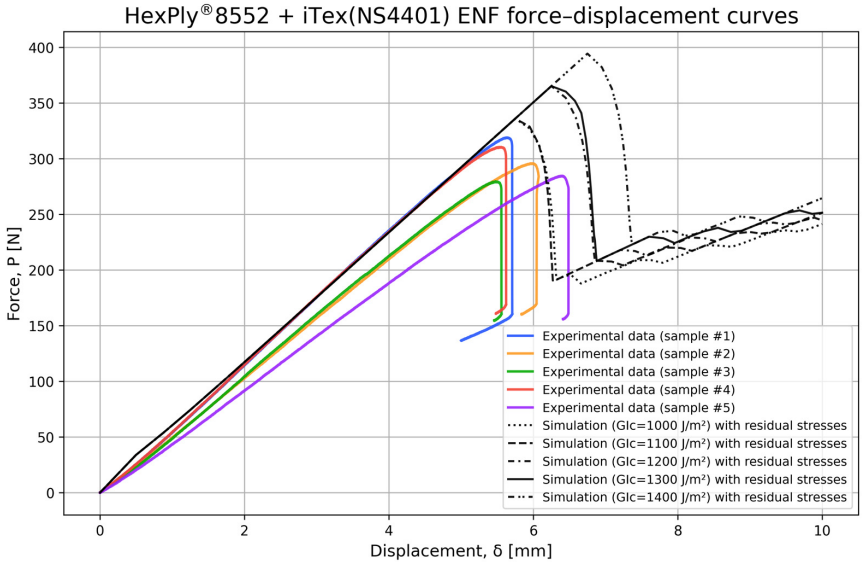

Figure 18. Experimental and numerical load–displacement curve from DCB test for samples with iTex (NS4401) as thermoplastic interleaves.

It is important to note that the discussions above are based on several assumptions regarding the physics of crack growth in the experiments, as well as assumptions inherent in the numerical simulations. In quasi-isotropic laminates such as the one studied here, DCB and ENF tests may induce not only delamination growth but also intraply damage, such as ply cracking in the off-axis plies. These intraply forms of damage can reduce the stiffness of the plies and, consequently, the overall laminate stiffness, affecting both the evaluation of fracture energies and the influence of thermal residual stresses. However, because the off-axis plies are very thin (0.166 mm) compared to the central 0° plies (1.66 mm) and because the primary stiffness in DCB and ENF tests is dominated by the axial response, these effects are assumed to be negligible.

Another assumption is that the nanofiber interleaf layers have a negligible influence on the global laminate stiffness. The interface enTex and iTex layers is extremely thin and they have much lower stiffness than the carbon/epoxy plies, both relative to the individual ply thickness and overall laminate thickness. Additionally, these layers are positioned at the laminate mid-plane, so their contribution to the global bending stiffness is minimal and can safely be neglected.

In evaluating the effects of thermal residual stresses, it is assumed that the composite laminate is thin and can be modeled using classical laminate plate theory. This implies that out-of-plane normal and shear deformations are neglected when correcting for thermal residual stresses. However, because the apparent energy release rates are determined from actual experimental measurements rather than purely from classical formulas, these deformation effects are partially captured in the results.

In the numerical simulations, mechanisms such as fiber bridging or any other processes beyond crack growth are excluded. The virtual crack closure technique, based on linear elastic fracture mechanics, is used to simulate delamination. While the overall deformation

of the carbon/epoxy laminate is reasonably linear, microscopic nonlinear effects are present but neglected in the current simulation approach.

Finally, the effect of nanofiber interleaf layers in the simulations is incorporated by assuming higher fracture toughness in both Mode I and Mode II. Although electrospun nanofiber interleafs enhance fracture toughness, the underlying microscopic mechanisms, such as fiber bridging, pull-out, ductile deformation, or crack deflection, are not explicitly modeled. Instead, their effect is represented solely through the increased macroscopic fracture toughness.

4. Conclusions

This study investigated the effect of electrospun thermoplastic nanofiber interleaves (enTex and iTex grades NS4001 and NS4401) on the interlaminar fracture toughness of HexPly® 8552 composites. Mode I and Mode II delamination resistance were characterized experimentally using standardized DCB and ENF test configurations on a symmetric quasi-isotropic laminate $[-45/45/90/0_5]_s$ containing a thick unidirectional 0° ply at the mid-plane. The influence of thermally induced residual stresses was explicitly considered in the fracture toughness evaluation. The experimental results confirm that nanofiber interleaving significantly enhances delamination toughness in both fracture modes. The baseline laminate without nanofiber interleaves exhibited an average Mode I fracture toughness of approximately 160 J/m^2, while the incorporation of electrospun veils increased G_{Ic} by +138.5% for enTex, +87.3% for iTex NS4001, and +132.0% for iTex NS4401. Similarly, Mode II fracture toughness was substantially improved, with increases in G_{IIc} of +116.9% for enTex, +244.5% for iTex NS4001, and +92.5% for iTex NS4401, demonstrating the strong effectiveness of nanofiber interleaves, particularly under shear-dominated loading. The magnitude of the improvements observed is in line with the latest literature and exceeds what is typically achievable with traditional thermoplastic particle interleaving. While enTex and iTex are composed of different base polymers, both feature nanoscale fibers with an extensive surface area that significantly improves the interfacial interaction with their respective resin systems. Specifically, the iTex base polymer incorporates a high density of reactive groups within the polymer chain; this chemical functionality, combined with the substantial surface area inherent to the nanofibrous morphology, contributes to its exceptional fracture toughness performance. Another outcome of this work is the quantitative assessment of thermal residual stress effects on the DCB and ENF fracture toughness measurements in quasi-isotropic laminates. Accounting for these stresses increased the apparent fracture toughness values by an average of 94 J/m^2 in Mode I and 180 J/m^2 in Mode II. These corrections highlight that residual stresses represent a non-negligible contribution to the measured energy release rates and should be included when using multidirectional laminate in DCB and ENF tests. Finite element simulations using VCCT-based interface modeling showed good agreement with the experimentally observed load–displacement responses and crack initiation loads when corrected fracture toughness values were applied. This supports the validity of the experimental methodology and the residual stress correction approach. Overall, the results demonstrate that electrospun thermoplastic nanofiber interleaves provide an effective and scalable route for improving the damage tolerance of advanced CFRP laminates. Future work should focus on detailed fractographic analysis to identify the dominant toughening mechanisms and on extending the approach toward multifunctional interleaves for structural composite applications. Recent innovations such as the electrically modified iTex system indicate a future direction where nanofiber interleaves can also function as in situ sensors. These smart materials provide real-time damage awareness, aligning with predictive maintenance goals in aerospace and wind energy sectors.

Author Contributions: M.S.: sample manufacturing, experimenting, formal analysis, writing original draft, review and editing. A.Y.: investigation, review and editing; N.S.: review and editing. H.H.: review and editing. P.A.: review and editing. F.T.: review and editing. E.E.: review and editing. M.H.: methodology, modeling, formal analysis, writing, review and editing. C.B.: conceptualization, administration, supervision, funding acquisition. All authors have read and agreed to the published version of the manuscript.

Funding: This research was supported by the national funded project ISurface (Grant Number 109.442 INT-ENG), which was supported by Innosuisse, Swiss Innovation Promotion Agency.

Data Availability Statement: The data presented in this study are available upon request from the corresponding author.

Acknowledgments: We would like to thank Fabio Pavia, Thomas Hirche and Rene Roos from the company Ansys for the support in this study related to the simulation activities.

Conflicts of Interest: Ata Yoosefinejad and Naresh Sanandiya were employed by Munro Technology Limited; Hamed Heravi and Peyman Adl were employed by Z-Prime; Frederick Tischhauser and Edgars Eglitis were employed by Axalp Technologies AG. The remaining authors declare that the research was conducted in the absence of any commercial or financial relationships that could be construed as a potential conflict of interest.

References

1. París, F.; Blázquez, A.; McCartney, L.N.; Barroso, A. Characterization and Evolution of Matrix and Interface Related Damage in [0/90]S Laminates under Tension. Part II: Experimental Evidence. *Compos. Sci. Technol.* **2010**, *70*, 1176–1183. [CrossRef]
2. Hajikazemi, M.; Ahmadi, H.; McCartney, L.N.; Van Paepegem, W. A Variational Approach for Accurate Prediction of Stress and Displacement Fields and Thermo-Elastic Constants in General Symmetric Laminates Containing Ply Cracking and Delamination under General Triaxial Loading. *Int. J. Solids Struct.* **2022**, 254–255, 111917. [CrossRef]
3. De Castro Saiki, L.E.; Gomes, G.F. Understanding and Mitigating Delamination in Composite Materials: A Comprehensive Review. *Mech. Adv. Mater. Struct.* **2024**, *31*, 13147–13167. [CrossRef]
4. Huang, T.; Bobyr, M. A Review of Delamination Damage of Composite Materials. *J. Compos. Sci.* **2023**, *7*, 468. [CrossRef]
5. Zhu, R.; Liu, Y.; Nie, X.; Xiao, Q.; Liang, J.; Cao, D. Compressive Failure and Dual-Defect Coupling Effects of Open-Hole Composite Laminates with Drilling-Induced Delamination. *Materials* **2025**, *18*, 2790. [CrossRef]
6. Varna, J.; Freire, R.T.S.; Loukil, M.S.; Al-Ramahi, N.J. COD and CSD Based Model for In-Plane Stiffness of Symmetric Laminates with Cracks in Plies and Local Delaminations: Analysis of Crack Face Sliding. *Compos. Part A Appl. Sci. Manuf.* **2025**, *189*, 108594. [CrossRef]
7. McCartney, L.N. Approximate Method of Predicting Ply Crack Formation in General Symmetric Laminates Subject to Biaxial Loading and Bending. In Proceedings of the 13th European Conference on Composite Materials (ECCM-13), Stockholm, Sweden, 2–5 June 2008.
8. Elder, D.J.; Thomson, R.S.; Nguyen, M.Q.; Scott, M.L. Review of Delamination Predictive Methods for Low Speed Impact of Composite Laminates. *Compos. Struct.* **2004**, *66*, 677–683. [CrossRef]
9. Patel, P.; Chaudhary, V. Delamination Evaluation in Drilling of Composite Materials—A Review. *Mater. Today Proc.* **2022**, *56*, 2690–2695. [CrossRef]
10. Bak, B.L.V.; Sarrado, C.; Turon, A.; Costa, J. Delamination Under Fatigue Loads in Composite Laminates: A Review on the Observed Phenomenology and Computational Methods. *Appl. Mech. Rev.* **2014**, *66*, 060803. [CrossRef]
11. Zou, Y.; Tong, L.; Steven, G.P. VIBRATION-BASED MODEL-DEPENDENT DAMAGE (DELAMINATION) IDENTIFICATION AND HEALTH MONITORING FOR COMPOSITE STRUCTURES—A REVIEW. *J. Sound Vib.* **2000**, *230*, 357–378. [CrossRef]
12. Burhan, M.; Ullah, Z.; Kazancı, Z.; Catalanotti, G. A Critical Review on Free Edge Delamination Fracture Criteria. *Mech. Adv. Mater. Struct.* **2024**, *31*, 13542–13555. [CrossRef]
13. Zeng, Y.; Liu, H.-Y.; Mai, Y.-W.; Du, X.-S. Improving Interlaminar Fracture Toughness of Carbon Fibre/Epoxy Laminates by Incorporation of Nano-Particles. *Compos. Part B Eng.* **2012**, *43*, 90–94. [CrossRef]
14. Chen, B.; Cai, H.; Mao, C.; Gan, Y.; Wei, Y. Toughening and Rapid Self-healing for Carbon Fiber/Epoxy Composites Based on Electrospinning Thermoplastic Polyamide Nanofiber. *Polym. Compos.* **2022**, *43*, 3124–3135. [CrossRef]
15. Fikry, M.J.M.; Iizuka, K.; Nakatani, H.; Yoneyama, S.; Vinogradov, V.; Koyanagi, J.; Ogihara, S. Suppression of Delamination in CFRP Laminates with Ply Discontinuity Using Polyamide Mesh. *J. Compos. Sci.* **2025**, *9*, 414. [CrossRef]

16. Knopp, A.; Scharr, G. Compression Properties of Z-Pinned Carbon-Fibre/Epoxy Laminates Reinforced with Circumferentially Notched z-Pins. *Compos. Sci. Technol.* **2021**, *201*, 108486. [CrossRef]
17. Ou, Y.; González, C.; Vilatela, J.J. Understanding Interlaminar Toughening of Unidirectional CFRP Laminates with Carbon Nanotube Veils. *Compos. Part B Eng.* **2020**, *201*, 108372. [CrossRef]
18. Cheng, C.; Zhang, C.; Zhou, J.; Jiang, M.; Sun, Z.; Zhou, S.; Liu, Y.; Chen, Z.; Xu, L.; Zhang, H.; et al. Improving the Interlaminar Toughness of the Carbon Fiber/Epoxy Composites via Interleaved with Polyethersulfone Porous Films. *Compos. Sci. Technol.* **2019**, *183*, 107827. [CrossRef]
19. Jiao, W.; Niu, G.; Bai, D.; Zheng, Y.; Wang, H.; Liu, Y. Interlaminar Toughness of Carbon Fiber/Epoxy Laminates Interleaved by Nanofibrous Veils: From Molecular Structure to Macroscopic Properties. *Compos. Sci. Technol.* **2025**, *267*, 111205. [CrossRef]
20. Lu, T.; Xue, L.; Ning, H.; Wu, X.; Ding, Z.; Hu, N.; Zhao, L.; Qi, X. Optimizing Thickness and Interlayer Placement of Electrospun TPU Nanofibrous Membranes for Enhanced Interlaminar Performance and Impact Resistance in CFRP Laminates. *Polym. Compos.* **2025**, *47*, 646–661. [CrossRef]
21. Priasso, V.; Lamon, J.; Ha-Minh, C.; Ladevèze, P.; Petiot, C. Experimental and Numerical Study of Crack Propagation in an Interleaved Laminate Reinforced by Thermoplastic Particles. *Compos. Part B Eng.* **2025**, *306*, 112654. [CrossRef]
22. Mohammadi, R.; Akrami, R.; Assaad, M.; Imran, A.; Fotouhi, M. Comparative Analysis of Delamination Resistance in CFRP Laminates Interleaved by Thermoplastic Nanoparticle: Evaluating Toughening Mechanisms in Modes I and II. *Compos. Part C Open Access* **2024**, *15*, 100518. [CrossRef]
23. Ramji, A.; Xu, Y.; Grasso, M.; Yasaee, M.; Webb, P. Effect of Interfacial Fibre Orientation and PPS Veil Density on Delamination Resistance of 5HS Woven CFRP Laminates under Mode II Loading. *Compos. Sci. Technol.* **2021**, *207*, 108735. [CrossRef]
24. Akbolat, M.Ç.; Wang, S.; Katnam, K.B.; Potluri, P.; Soutis, C. Low-Velocity Impact Response of Carbon/Epoxy Laminates with Interlaminar Hybrid Toughening via Core–Shell-Rubber Particles and Non-Woven Thermoplastic Fibre Veils. *Compos. Part A Appl. Sci. Manuf.* **2025**, *195*, 108944. [CrossRef]
25. Zhang, N.; Jiang, W.; Fu, Y.; Sun, Y.; Zhang, Z.; Zhao, D.; Li, S.; Di, C.; Yang, T.; Qiao, K. Fatigue Performance of CFRP Enhanced by Electrospun PA6 Nanofiber Films. *J. Taiwan Inst. Chem. Eng.* **2025**, *176*, 106327. [CrossRef]
26. Wang, C.; Wang, W.; Qi, H.; Dai, Y.; Jiang, S.; Ding, B.; Wang, X.; Li, C.; Zeng, J.; Wu, T.; et al. Electrospinning and Electrospun Nanofibers: From Academic Research to Industrial Production. *Prog. Mater. Sci.* **2025**, *154*, 101494. [CrossRef]
27. Mahato, B.; Lomov, S.V.; Shiverskii, A.; Owais, M.; Abaimov, S.G. A Review of Electrospun Nanofiber Interleaves for Interlaminar Toughening of Composite Laminates. *Polymers* **2023**, *15*, 1380. [CrossRef]
28. Guo, S.; Dillard, D.A.; Nairn, J.A. Effect of Residual Stress on the Energy Release Rate of Wedge and DCB Test Specimens. *Int. J. Adhes. Adhes.* **2006**, *26*, 285–294. [CrossRef]
29. Yokozeki, T.; Ogasawara, T.; Aoki, T. Correction Method for Evaluation of Interfacial Fracture Toughness of DCB, ENF and MMB Specimens with Residual Thermal Stresses. *Compos. Sci. Technol.* **2008**, *68*, 760–767. [CrossRef]
30. *ASTM D55028-01*; Standard Test Method for Mode I Interlaminar Fracture Toughness of Unidirectional Fiber-Reinforced Polymer Matrix Composites1. ASTM International: West Conshohocken, PA, USA, 1994.
31. Russell, A.; Street, K. Moisture and Temperature Effects on the Mixed-Mode Delamination Fracture of Unidirectional Graphite/Epoxy. In *Delamination and Debonding of Materials*; ASTM International: West Conshohocken, PA, USA, 1985; pp. 349–370, ISBN 978-0-8031-0414-3.
32. Nairn, J.A. On the Calculation of Energy Release Rates for Cracked Laminates with Residual Stresses. *Int. J. Fract.* **2006**, *139*, 267–293. [CrossRef]
33. Nairn, J.A. Fracture Mechanics of Composites With Residual Thermal Stresses. *J. Appl. Mech.* **1997**, *64*, 804. [CrossRef]
34. Data Sheet: HexPly® 8552 Epoxy Matrix (180 °C/356 °F Curing Matrix). Available online: https://satsearch.co/products/hexcel-corporation-hex-ply-8552-epoxy-matrix-180deg-c-356deg-f-curing-matrix (accessed on 1 February 2026).
35. Nettles, A.T.; Scharber, L. The Influence of G_I and G_{II} on the Compression after Impact Strength of Carbon Fiber/Epoxy Laminates. *J. Compos. Mater.* **2018**, *52*, 991–1003. [CrossRef]
36. Lai, J.; Yu, Y.; Zhang, X.; Qiang, W.; Zhang, X. Interlaminar Fracture Toughness and Impact Resistance of Carbon Fiber Reinforced Composite with Magnetic Aligned CNTs. *Compos. Part B Eng.* **2025**, *291*, 112008. [CrossRef]
37. Palazzetti, R.; Zucchelli, A.; Gualandi, C.; Focarete, M.L.; Donati, L.; Minak, G.; Ramakrishna, S. Influence of Electrospun Nylon 6,6 Nanofibrous Mats on the Interlaminar Properties of Gr–Epoxy Composite Laminates. *Compos. Struct.* **2012**, *94*, 571–579. [CrossRef]